

Design and Evaluation of a Passive Compliance Control Method of an Offshore Wind Turbine Blade Grinding Robot

Xinrong Liu ✉ – Hao Li – Yu Fang – Diqing Fan

Shanghai University of Engineering Science, School of Mechanical and Automotive Engineering, China

✉ lxr4849@126.com

Abstract Robots that repair offshore wind turbine blades are susceptible to interference from different factors such as external wind, which can lead to damage to the blades by the robot during the grinding process. Therefore, the robot needs to keep the grinding contact force constant in the complex operating environment. In this study, a constant force control device that is based on a pneumatic system is designed to address this problem, and a controller that is based on an improved Active Disturbance Rejection Control (ADRC) algorithm was proposed to control this device. Based on the analysis of the mechanism of the constant force control device and according to the relative order of the system, a second-order ADRC is designed. The controller utilizes a tracking differentiator (TD) to filter the input signal, an extended state observer (ESO) to estimate the total perturbation in the system, and a nonlinear state error feedback control law (NLSEF) for compensation. In order to solve the problems of electric proportional valve dead-zone characteristics, unknown interference during high altitude operation, tilt angle changes during grinding, dead-zone compensation, and gravity compensation algorithms were incorporated into the controller. Finally, the experimental platform is built to carry out experiments under various working conditions. The experimental results show that the controller improves the system regulation time by 59%, with an overshoot close to zero, when compared with the traditional proportional-integral-derivative (PID) algorithm. Also, both the absolute value of the maximum error and the mean square value of the error have been reduced to a large extent. As a result, the controller has a better force control accuracy and dynamic tracking performance, strong interference rejection capability and adaptability, and provides a theoretical basis for practical engineering applications.

Keywords improved active disturbance rejection control, gravity compensation, dead-zone compensation, offshore wind turbine blade, pneumatic loading system

Highlights

- Design and mathematical model of a pneumatic constant force control device are presented.
- A controller based on an improved ADRC algorithm is proposed.
- Dead-band compensation and gravity compensation algorithms are added to the controller.
- The improved ADRC has better responsiveness, control accuracy, and immunity to interference.

1 INTRODUCTION

With the massive consumption of fossil fuels, the problems of environmental degradation, climate warming, and the energy crisis have become more serious [1]. As well, offshore wind energy, as one of the very promising renewable and clean energy sources, can alleviate the energy pressure to a great extent [2,3]. The global offshore wind capacity has grown rapidly over the last decade [4]. China's installed offshore wind capacity was 35.6 GW by the end of 2023. The increase in installed offshore wind capacity means that some of the installed wind turbines are ageing and so maintenance of the wind turbine equipment is very important [5]. The first maintenance of the blades should be carried out after the offshore wind turbine has been dynamically commissioned and has been in normal operation for 7 to 10 days, and then every 6 months. Offshore wind turbine blades, are key components of the wind turbine system, and are at the heart of wind turbine equipment repair [6], with repair costs accounting for 20 % to 25 % of the total average cost [7]. This includes losses due to downtime for maintenance and labor costs. Currently, offshore wind turbine blade surface repair primarily relies on manual labor with the following problems: first, the high-risk factor of overhead operation, high labor intensity, a grinding process where there is great noise and a significant amount of dust, and long-term work in this environment tends to lead to earlier suffering

from occupational diseases. Second, the blade grinding quality is not stable, with an artificial grinding blade that has uneven quality. Third, blade maintenance incurs higher costs, and fourth, low efficiency. In order to solve the problems of manual repair, the use of robots instead of manually repairing the wind turbine blades is a good solution [8,9]. In comparison to manual repair of an offshore wind turbine blade, robotic repair has the advantages of high safety and efficiency [10].

If a robot is utilized in the blade polishing process, where the end of the polishing tool and blade contact generates the contact force, that contact force is too small and leads to a blade polishing quality that cannot meet the requirements. It should be noted that if the contact force is too large, an overcutting phenomenon damage to the surface of the blade will appear. Therefore, the size of the sanding force directly determines the quality of the processed workpiece, and how to maintain a constant sanding contact force has become a key issue to be solved by robot grinding. Current robotic constant force control methods include active compliance control and passive compliance control [11].

The essence of active compliance control is that the robot feeds back on the contact force signal and adopts a corresponding active control strategy to keep the contact force constant by adjusting the position, speed, and acceleration of the robot end, thus realizing the force compliance control of the grinding process. Guo et al. [12]

and Lakshminarayanan et al. [13] propose an adaptive variable, impedance active, compliance constant force control method, and an iterative learning controller based on impedance control. Zhang et al. [14] proposed a force-position anti-disturbance control strategy based on fuzzy proportional-integral-derivative (PID) control. Zhang et al. [15] proposed a constant force control based on active disturbance rejection control theory. However, when encountering unknown wind disturbances in blade grinding for offshore wind turbines, it is difficult to maintain the control accuracy regardless of whether impedance control or force-position hybrid control is adopted.

In order to cope with the problem of external disturbances, the researchers developed a force control end-effector [16-24], which achieves contact force control by means of passive compliance control. Wei and Xu [16] proposed the always symmetric structure to avoid the vibration caused by an eccentric force. Zhang et al. [17] utilized the second bending mode of fixed-guided compliant beams to design the compliance constant force mechanism. Chen et al. [18] and Xu et al. [19] designed a magnetic vibration absorber and integrated them into a smart end-effector for force control. Li et al. [20] and Mohammad et al. [21] use servo motors and a voice coil actuator, respectively, to design the end-effector to realize the control of the grinding contact force, but the force control is difficult. Liang et al. [22] and Huang et al. [23] used a low friction air cylinder to design the end-effector and used a PID algorithm to control it. Even though this compliance is better, the control accuracy is lower.

In order to solve the force control accuracy to improve the disturbance rejection capability, this study developed an end-effector using a low-friction cylinder. Also, an improved ADRC algorithm combining dead-zone compensation algorithm and a gravity compensation algorithm is proposed as the controller of this device, according to the principle of ADRC [24-26]. The algorithm not only solves the problems of the dead zone characteristics of the electric proportional valve and the change of the tilt angle during the grinding process, but also effectively copes with the problem of the unknown wind interference during high-altitude operation. Finally, the authors conclude that through experimental verification the adjustment of system time is less, the maximum deviation is lower, and the tracking error is smaller under the improved ADRC algorithm. Therefore, it can be surmised that compared to the PID algorithm, the improved ADRC has better dynamic response performance, force control accuracy, and anti-interference ability.

2 METHODS AND MATERIALS

The robot is lifted by the lifting mechanism to the vicinity of the blade, then guided by a traction rope where the robot adheres to the blade by a bottom vacuum suction cup, and after that it can begin the repair work on the blade. Fig. 1 shows the schematic diagram of robotic grinding, where the robot grinds the area to be repaired by guiding the end-effector.

2.1 Composition and Working Theory of an End-effector

The schematic diagram of the end-effector is shown in Fig. 2, and its main parts are: an air compressor, a pneumatic filter and regulator (F.R.), a 5-way 2-position pneumatic solenoid valve, an electrical proportional valve, a pneumatic cylinder, an inclination sensor, a force sensor, a STM32, a host computer, etc. The end-effector collects the grinding contact force through the force sensor, and the improved ADRC algorithm controls the opening of the electric proportional valve according to the pressure feedback value so as to achieve the expansion and contraction of the cylinder, and to ultimately achieve control of the grinding contact force.

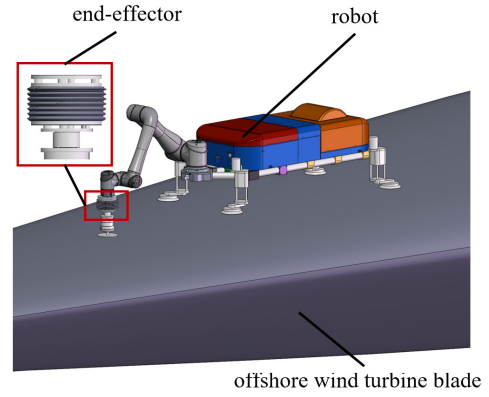


Fig. 1. Schematic Diagram of Robot Grinding

2.2 Modelling of the End-effector

From the composition and working theory of the end-effector, it can be seen that the end-effector is mainly composed of an electrical proportional valve, a cylinder, connecting air tubes, and force feedback in four parts. These four parts need to be modelled next.

2.2.1 Modelling of the Electrical Proportional Valve

The flow rate through the valve port of an electrical proportional valve is related to the flow area of the valve port and the magnitude of the inlet and outlet pressures. Approximating the gas flow at the valve port as a one-dimensional isentropic flow of an ideal gas, with the SANVILLE gas flow formula, the following formula is derived:

$$q = C_q A_q p_0 \sqrt{\frac{2}{RT}} \varphi \left(\frac{P_1}{P_0} \right) = C_q w_{x_v} p_0 \sqrt{\frac{2}{RT}} \varphi \left(\frac{P_1}{P_0} \right). \quad (1)$$

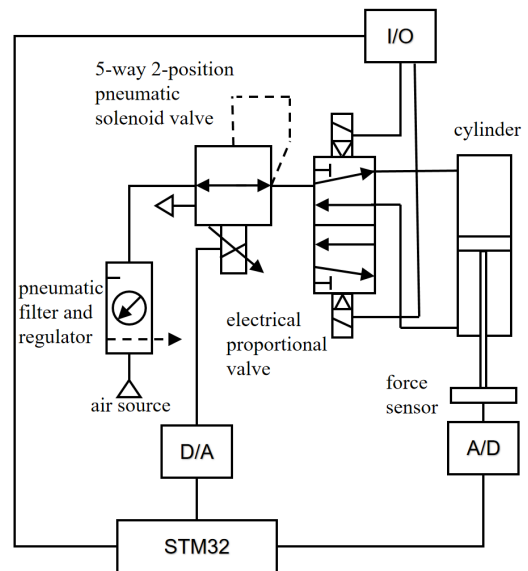


Fig. 2. Schematic diagram of the end-effector

$$\varphi \left(\frac{P_1}{P_0} \right) = \begin{cases} \left(\frac{2}{k+1} \right)^{1/(k-1)} \sqrt{\frac{k}{k+1}}, & 0 \leq \frac{P_1}{P_0} \leq C_i \\ \sqrt{\frac{k}{k-1} \left(\left(\frac{P_1}{P_0} \right)^{2/k} - \left(\frac{P_1}{P_0} \right)^{(k+1)/k} \right)}, & C_i \leq \frac{P_1}{P_0} \leq 1 \end{cases}, \quad (2)$$

$$C_i = \left(\frac{2}{k+1} \right)^{\frac{k}{k-1}}, \quad (3)$$

q is the mass flow rates into the electrical proportional valve; C_q is the flow coefficient; A_q is the orifice open area of the electrical proportional valve; w is the electrical proportional valve opening area gradient; x_v is the electrical proportional valve spool displacement; p_0 is the electrical proportional valve inlet pressure; p_1 is the electrical proportional valve outlet pressure; R is the universal gas constant; T is the absolute temperature; C_i is the critical pressure ratio; k is the isentropic constant; and k is taken to be 1.4, [27].

Electrical proportional valves are electrically driven spools to achieve continuous control of the flow rate. When the supply port pressure and the temperature inside the valve is unchanged, the electrical proportional valve spool displacement and the input voltage can be equated into a proportional link, the following formula is derived:

$$x_v = e_v u_v, \quad (4)$$

where e_v is the electrical proportional valve flow gain and u_v is the control voltage.

2.2.2 Modelling of the Cylinder

The gas flows out of the electric proportional valve and into the cylinder, according to the law of conservation of energy:

$$\begin{cases} q_{ma} = \frac{dm_a}{dt} = \frac{d(\rho V_a)}{dt}, \\ q_{mb} = \frac{dm_b}{dt} = \frac{d(\rho V_b)}{dt}, \end{cases} \quad (5)$$

where q_{ma} is the inflow cylinder gas mass flow rate; q_{mb} is the outflow cylinder gas mass flow rate; m_a is the inflow cylinder gas mass; m_b is the outflow cylinder gas mass; V_a is the rod end volume; and V_b is the rear end volume.

Assume that the gas is an ideal gas and satisfies the formula:

$$P_d = \rho RT, \quad (6)$$

where P_d is the gas pressure in the cylinder; ρ is the gas density in the cylinder, and T is the gas temperature in the cylinder.

Assuming that the spool pushes the cylinder downward, the cylinder displacement is x ; and the cylinder stroke is l . From Eq. (6), it follows that:

$$\begin{cases} q_{ma} = P_a \dot{x} \frac{A_a}{RT} + \dot{P}_a \frac{(l/2+x)}{kRT}, \\ q_{mb} = -P_b \dot{x} \frac{A_b}{RT} + \dot{P}_b \frac{(l/2-x)}{kRT}, \end{cases} \quad (7)$$

where k is the adiabatic index, $k=1.4$; A_a is the contact area of the without rod chamber of the cylinder; and A_b is the contact area of the with rod chamber.

2.2.3 Modelling of the Pneumatic Hose

The gas flow from the electric proportional valve passes through a pneumatic hose of length L and enters the chamber of the cylinder without a rod. The gas flow in the tube is equal to the outlet flow of the proportional valve. According to Anderson's theory, Eq. (8) is derived:

$$q = K_1(P_1 - P_2), \quad (8)$$

$$K_1 = \frac{\rho_v D^2}{32\mu L} A, \quad (9)$$

where q is the gas mass flow rate of the g pneumatic hose; P_1 is the inlet pressure of the pneumatic hose; P_2 is the outlet pressure of the pneumatic hose; ρ_v is the average density of the system gas; D is the

inner diameter of the gas pipe; μ is the viscosity coefficient of the system gas; and A is the cross-sectional area of the pneumatic hose. From Eqs. (1), (7) and (8), it follows that:

$$\begin{cases} \dot{P}_a = \frac{-kP_a \dot{x} A_a}{(l/2+x)} + \frac{kRTC_q W x_v P_0 H_0 \varphi (P_a / (P_1 - q / K_1))}{(l/2+x)}, \\ \dot{P}_b = \frac{kP_b \dot{x} A_b}{(l/2-x)} - \frac{kRTC_q W x_v P_0 H_0 \varphi (P_b / (P_1 - q / K_1))}{(l/2-x)}. \end{cases} \quad (10)$$

2.2.4 Modelling of the Force Sensor

The force sensor belongs to the resistive type sensors, and is considered as an equivalent proportional element, from which Eq. (11) is derived:

$$u = K_u F, \quad (11)$$

u is the output voltage; K_u is the voltage gain; and F is the detection pressure.

Since the force transducer has a good linear relationship, it is linearized and the following formula is derived.

$$F = K_m x, \quad (12)$$

K_m is the pressure gain; x is the output signal.

2.2.5 End-effector Force Balance Analysis

The end-effector force sketch is shown in Fig. 3. According to Newton's second theorem, without considering the effect of cylinder friction, and the cylinder piston force, the balance equation is:

$$P_a A_a - P_b A_b = m\ddot{s} + B\dot{s} + F_n, \quad (13)$$

where A_a is the contact area of the rear end of the pneumatic cylinder and A_b is the contact area of the rod end; P_a is the rear end of the cylinder pressure; P_b is the rod end pressure; m is the cylinder piston and load total mass; \dot{s} is the cylinder piston moving speed; \ddot{s} is the cylinder piston moving acceleration; B is the damping coefficient; F_n is the end-effector grinding contact force.

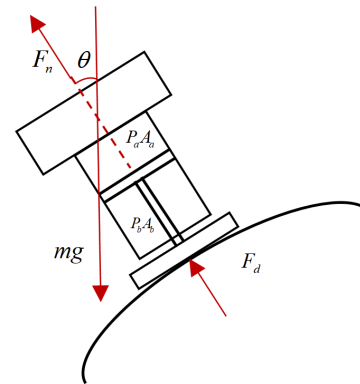


Fig. 3. Schematic diagram of the end-effector

When the robot performs grinding work, the spatial attitude changes in real time, and the grinding contact force collected by the force sensor has a large error due to the gravity effect of the end-effector. Therefore, it is necessary to design a gravity compensator to eliminate the gravity influence of the end-effector along the force control direction. The force analysis of the end-effector is shown in Fig. 3, where mg is the gravity of the end-effector, F_d is the force measured by the force sensor, and θ is the angle between the gravity and the force measured by the force sensor. Therefore, the actual output force F_n is:

$$F_n = F_d + mg \cos \theta. \quad (14)$$

When the end-effector is in contact with the blade, the axial force is F_n , the resulting displacement is y , and the equivalent stiffness model coefficient is K_e , the following formula is derived:

$$F_n = K_e y. \tag{15}$$

From Eqs. (13-15), it follows that:

$$P_a A_a - P_b A_b = M\ddot{s} + B\dot{s} + K_e y. \tag{16}$$

To facilitate the analysis and design of the controller, from Eqs. (1-16). If we define the state variable $F = x_1, \dot{F} = x_2, P_a = x_3, P_b = x_4, x_v = u$, then the system state space equation set is obtained as:

$$\begin{cases} \dot{x}_1 = x_2 \\ \dot{x}_2 = K_n (A_a x_3 - A_b x_4 - B\dot{s} - K_e y) \\ \dot{x}_3 = \frac{-kP_a \dot{x}_A_a + \frac{kRTC_q W x_v P_0 H_0 \phi(P_a / (P_1 - q / K_1))}{(l / 2 + x)}}{(l / 2 + x)} \\ \dot{x}_4 = \frac{kP_b \dot{x}_A_b - \frac{kRTC_q W x_v P_0 H_0 \phi(P_b / (P_1 - q / K_1))}{(l / 2 - x)}}{(l / 2 - x)} \\ y = x_1 \end{cases} \tag{17}$$

3 IMPROVED ADRC CONTROLLER DESIGN

If we take Eq. (17), the end-effector model described as a 3rd order system, then according to the method of active disturbance rejection controller order selection [28], the relative order of the system is taken to be 2, the 3rd order is regarded as a perturbation, and the second-order nonlinear active disturbance rejection controller is designed and Eq. (17) is rewritten as:

$$\ddot{F} = \underbrace{f(\dot{F}, P_a, P_b, w, t)}_{w(t)} + bu, \tag{18}$$

where $w(\cdot)$ is a nonlinear function of the “total disturbance” of the end-effector, including the unmodelled portion, higher-order nonlinearities, and control gain estimation errors, and b is the control gain estimate.

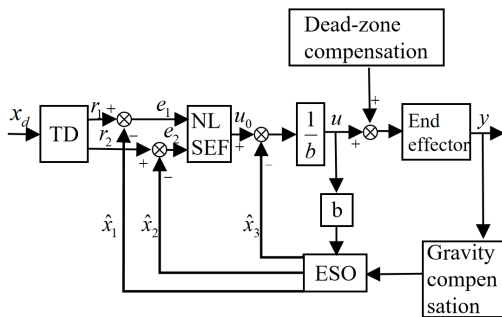


Fig. 4. End-effector controller

The improved ADRC controller consists of a tracking differentiator, a nonlinear state error feedback control law, an extended state observer, gravity compensation, dead-zone compensation of five parts, as shown in Fig. 4.

3.1 The Tracking Differentiator

The tracking differentiator is used to smooth the desired force and reduce the overshoot caused by excessive error. According to Han [28], the tracking differentiator (TD) is as follows:

$$\begin{cases} \dot{r}_1 = r_2 \\ \dot{r}_2 = fhan(r_1 - x_d, r_2, R, h) \end{cases} \tag{19}$$

where x_d is the desired force loading input signal; r_1 is the tracked value of the input signal x_d , and r_2 is the differential of the input signal x_d . The $fhan(z_1, z_2, R, h)$ function is as follows:

$$\begin{cases} d = Rh^2, a_0 = hz_2, y = z_1 + a_0 \\ a_1 = \sqrt{d(d + 8|y|)} \\ a_2 = a_0 + sign(y)(a_1 - d) / 2 \\ s_y = [sign(y + d) - sign(y - d)] / 2 \\ a = (a_0 + y - a_2)s_y + a_2 \\ s_a = [sign(a + d) - sign(a - d)] / 2 \\ fhan = -R[a / d - sign(a)]s_a - r_0 sign(a) \end{cases} \tag{20}$$

where z_1 and z_2 are the state quantities of the $fhan$; R and h are the control parameters of the $fhan$. R depends on the smoothing processing speed and the system capacity; the larger the value of R , the stronger the ability to track the input signal. The value of r is usually not infinite, and so it needs to be adjusted according to the actual situation. Additionally, h is the step size.

3.2 Extended State Observer

The extended state observer is used to estimate the total perturbation of the system in real time and is the central aspect of the active disturbance rejection control algorithm. The extended state observer (ESO) derives a state estimate \hat{x}_1, \hat{x}_2 of the desired signal and an estimate of the total disturbance \hat{x}_3 from the total disturbance $w(\cdot)$, output signals y and \dot{y} . The ESO design is as follows:

$$\begin{cases} e_0 = \hat{x}_1 - y \\ \dot{\hat{x}}_1 = \hat{x}_2 + \beta_1 e_0 \\ \dot{\hat{x}}_2 = \hat{x}_3 - \beta_2 fal(e_0, \alpha_1, h) + bu \\ \dot{\hat{x}}_3 = -\beta_3 fal(e_0, \alpha_2, h) \end{cases} \tag{21}$$

$\beta_1, \beta_2, \beta_3, \alpha_1, \alpha_2, h$ is the parameter of ESO and the $fal(\cdot)$ expression is as follows:

$$fal(e_0, \alpha, h) = \begin{cases} e_0 / h^{(1-\alpha)}, |e_0| \leq h \\ sign(e_0) \cdot |e_0|^\alpha, |e_0| \geq h \end{cases} \tag{22}$$

3.3 The Nonlinear State Error Feedback Control Law

The nonlinear state error feedback (NLSEF) is a nonlinear control combination used instead of the linear combination of the conventional PID controller. Combining the observations of ESO with the output of TD, the combination NLSEF is as follows:

$$\begin{cases} e_1 = r_1 - \hat{x}_1 \\ e_2 = r_2 - \hat{x}_2 \\ u_0 = k_p \cdot fal(e_1, \alpha_1, h) + k_d \cdot fal(e_2, \alpha_2, h) \end{cases} \tag{23}$$

where k_p and k_d are the NLSEF nonlinear combination coefficients, respectively. In order to reduce the model uncertainty and the effect of external perturbations, \hat{x}_3 is compensated to the control quantity with the compensation equation:

$$u = \frac{u_0 - \hat{x}_3}{b}. \tag{24}$$

3.4 The Dead-zone Compensator

The dead-zone compensation is an algorithm to make the spool of the electrical proportional valve jump out of the neutral dead-zone quickly and enter the control zone. The dead-zone model parameters

are obtained by experimental identification methods to achieve pre-compensation for a wide range of dead-zones. The dead band compensator is designed as follows:

$$u_f = \begin{cases} u + u_3, & 0 < u \\ u + u_4, & u \leq 0 \end{cases} \quad (25)$$

where u_f dead-zone compensation after the control amount; u_3 for the experimentally measured electrical proportional valve inlet minimum operating voltage; u_4 for the experimentally measured electrical proportional valve maximum operating voltage.

4 RESULTS AND DISCUSSION

When repairing offshore wind turbine blades, the external environment is very complex, and at the same time there will be wind and other disturbances in the high-altitude air to increase the difficulty of the whole grinding operation. The robot controls the end position in the sanding process while using the end-effector to correct the end contact force, so as to realize the decomposition of force control and position control in the grinding process. This makes it possible to complete offshore wind turbine blade grinding even when the entire grinding process is disturbed by the external environment. In order to verify the application of the improved ADRC algorithm in the real working environment, an experimental rig was built and simulated offshore wind turbine blade grinding experiments were carried out. The robot model is Elibot ec66 with a working radius of 914 mm and a repeat positioning accuracy of ± 0.02 mm. Both algorithms use image processing and vision-guided path-planning-based methods. The test bench is shown in Fig. 5, and the main components and parameters of the experiment are shown in Table 1.

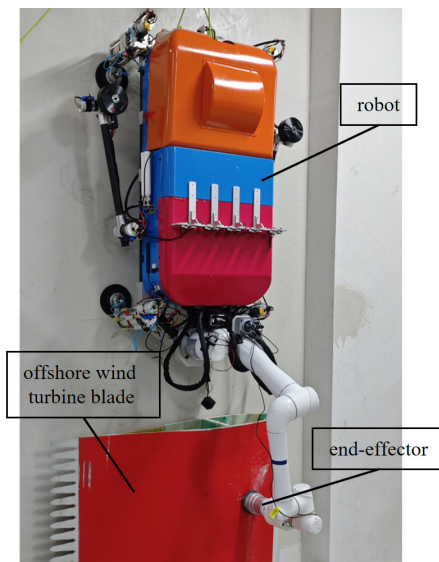


Fig. 5. Laboratory bench

Table 1. Key Components and Parameters

Component	Parameters
Air source	Outlet pressure: 1.0 MPa
F.R.	Set pressure: 0.9 MPa
Electrical proportional valve	Max. pressure: 0.9 MPa; Sensitivity: 0.2 %
Pneumatic cylinder	Stroke: 20 mm
Inclination sensor	Angular range: $\pm 90^\circ$; Repeatability: 0.5°
Force sensor	Capacity: 0 N - 100 N; Sensitivity: 0.1 %

4.1 Dead-zone Compensation Experiment

Firstly, it is verified whether the improved ADRC algorithm is able to compensate for the dead-zone effectively. Since the effect of the dead-zone is mainly manifested during commutation, a sinusoidal signal is used as the input signal. In the formula, where the input signal is $F = 60 + 10 \sin(1.257t)$, the amplitude is 20 N, and the force tracking curve and force tracking error curve are shown in Fig. 6. As can be seen in Fig. 6, the input signal can be tracked well with the dead-zone compensation algorithm; whereas without the dead zone compensation algorithm there is a hysteresis that leads to a large error. Therefore, this algorithm enables the controller to cross the dead-zone quickly and improves the dynamic performance of the system.

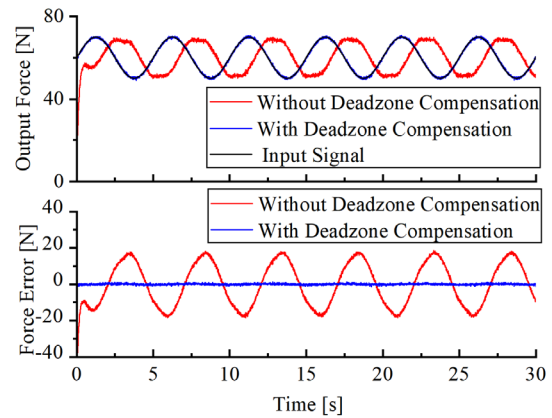


Fig. 6. Dead-zone compensation experiment

4.2 Gravity Compensation Experiment

When the end-effector is tilted, the grinding contact force is varied by the gravity of the device. This experiment, in order to verify the compensation effect of the gravity compensation algorithm, sets the desired force to 60 N, the grinding inclination angle is 0° to 90° , and the output force change curve is shown in Fig. 7. Without the gravity compensation algorithm, the output force error increases with the inclination angle, reaching a maximum of 18.7 N, while with the gravity compensation algorithm, the output force is smooth, and the maximum error is 2.3 N.

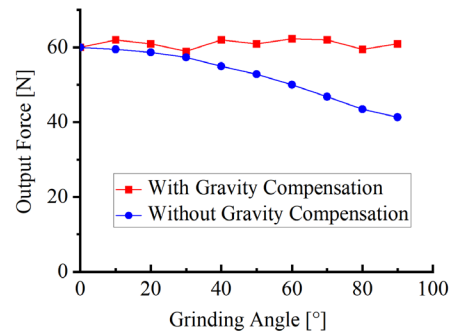


Fig. 7. Gravity compensation experiment

4.3 Constant Force Loading Experiment

The constant force loading experiment can test the transient response performance of the system. The desired force is set to $F = 60$ N according to the real grinding situation. The output force response curve and force tracking error curve are shown in Fig. 8. The system regulation time of the PID control is 1.83 s, with a maximum

overshoot of 10.93 %; while the system regulation time of the improved ADRC control is 0.75 s, with an overshoot close to zero. Therefore, the improved ADRC exhibits better transient response performance than PID control in the control system.

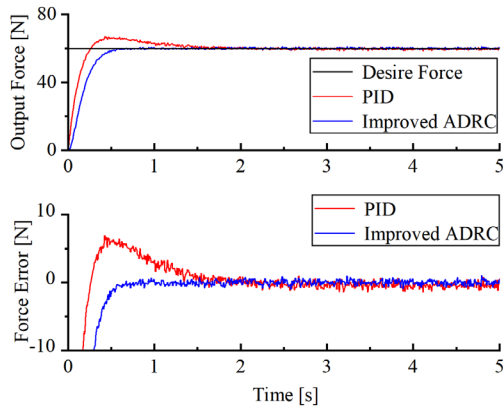


Fig. 8. Constant force loading experiment

4.4 Sinusoidal Force Loading Experiment

Sinusoidal loading experiments can test the dynamic performance of the whole system. The desired force is set to $F = 60 + 10 \sin(1.257t)$ in the experiment. The output force response curve and force tracking error curve are shown in Fig. 9. The maximum force tracking error is 5.2 N for PID control and 1.3 N for improved ADRC control. It can be obtained that the improved ADRC algorithm exhibits a smaller force tracking error, a smoother trend, and higher quality of control than PID control.

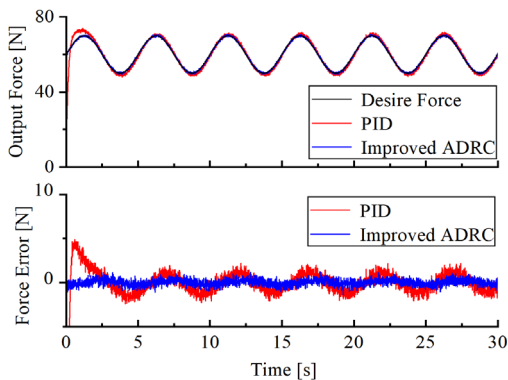


Fig. 9. Sinusoidal force loading experiment

4.5 Triangular Force Loading Experiment

Triangular force loading experiments can test the responsiveness of the system to sudden changes in the input signal. The triangular force signal has a period of 5, an amplitude of 20, and an initial value of 50. The output force response curve and force tracking error curve are shown in Fig. 10. It can be seen in the output force response curve and force tracking error curve that the PID control has some hysteresis when the force signal changes suddenly. Compared to the PID algorithm, the improved ADRC algorithm has a faster response and less force tracking error.

4.6 Trapezoidal Force Loading Experiment

Trapezoidal force loading can further test the fast performance and sudden change response performance of the controller, and the output force response curve and force tracking error curve are shown in

Fig. 11. When the direction of the loading signal changes abruptly, the control effect of the improved ADRC algorithm is significantly better than that of the PID algorithm, showing better anti-interference ability and stronger robustness.

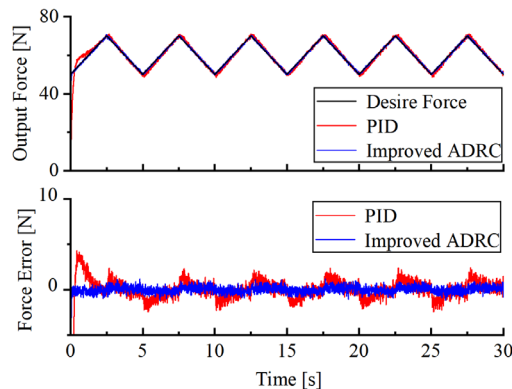


Fig. 10. Triangular force loading experiment

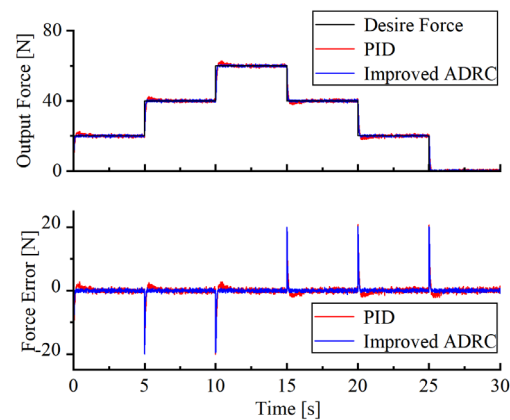


Fig. 11. Trapezoidal force loading experiment

4.7 Constant Force Loading Interference Experiment

In order to further verify the anti-disturbance performance of the improved ADRC algorithm, this experiment simulates the effects of the unknown wind disturbance and the deformation of the suction cup of the robot base at the high altitude. In the constant force loading process of two different algorithms, two different directions of disturbance forces are added. The output force response curves and force tracking error curves are shown in Fig. 12. From Fig. 12, it can be concluded that the improved ADRC algorithm is much stronger than the PID algorithm in the case of adding the same disturbance.

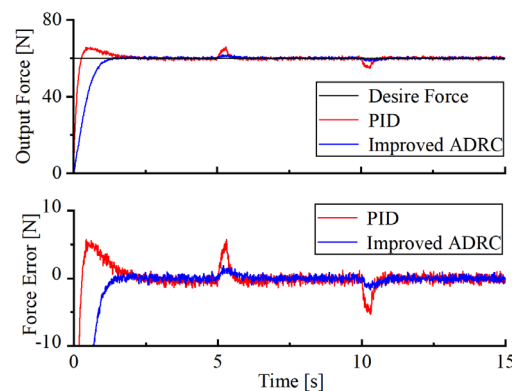


Fig. 12. Constant force loading interference experiment

Table 2. Performance indices

Control method	Performance indices	Constant loading	Sinusoidal loading	Triangular loading	Trapezoidal loading	Constant loading interference
PID	M_e	6.56	4.89	4.29	20.73	5.74
	μ_e	4.27	1.32	0.92	3.05	2.14
ADRC	M_e	0.52	1.24	1.14	20.16	1.89
	μ_e	0.12	0.13	0.13	2.59	0.26

4.8 Constant Force Loading Interference Experiment

In order to better quantitatively compare the two control algorithms, two sets of data, the absolute value of the maximum error M_e and the mean-square value of the error μ_e , are introduced for further illustration:

$$M_e = \max_{i=1,2,\dots,N} \{|e(i)|\}, \quad (26)$$

$$\mu_e = \frac{1}{N} \sum_{i=1}^N [e(i)]^2. \quad (27)$$

The results are shown in Table 2. Comparing the performance indicators from the Table 2, it can be seen that the absolute value of the maximum error and the mean square value of the error of the improved ADRC algorithm in several force loading experiments are smaller than that of the PID control. From this, the improved ADRC algorithm is superior to the PID control algorithm in terms of system regulation time, dynamic response ability, and anti-interference ability, which prove the effectiveness of the algorithm in the control of the contact force of end grinding of a high altitude wind turbine blade grinding robot.

5 CONCLUSIONS

In this paper, an end-effector based on passive flexible control is designed for the problems of unknown wind interference and deformation of suction cups at the robot base when the robot is grinding high-altitude wind turbine blades. The device is fixed at one end of the robot end while the other end fixes the grinding tool, effectively controlling the grinding contact force.

The end-effector adopts a pneumatic control system. Several problems such as electrical proportional valve dead-zone, attitude transformation, and external interference appear. In this paper, by establishing a mathematical model of the control system and analyzing the influence of system parameters and dead-zone characteristics on force control accuracy, an improved third-order ADRC controller with dead-zone compensation and gravity compensation is designed. It not only solves the problems of system lag caused by dead zone and attitude transformation affecting the contact force, but also improves the anti-interference ability of the control system.

Finally, seven sets of experiments are conducted to make a comprehensive comparison of the control algorithms. It can be concluded that the improved ADRC algorithm is more stable, faster, and more accurate than the PID algorithm in terms of the robustness of the control system and the anti-interference ability.

References

- [1] Liu, L., Wu, M., Mao, Y., Zheng, L., Xue, M., Bing, L., et al. Offshore Wind Energy Potential in Shandong Sea of China Revealed by ERA5 Reanalysis Data and Remote Sensing. *J Clean Prod* 464 142745 (2024) DOI:10.1016/j.jclepro.2024.142745
- [2] Sun, Y., Ai, H., Li, Y., Wang, R., Ma, R. Data-driven Large-Scale Spatial Planning Framework For Determining Size And Location Of Offshore Wind Energy Development: A Case Study of China. *Appl Energ* 367 123388 (2024) DOI:10.1016/j.apenergy.2024.123388
- [3] Yang, W., Kim, K.H., Lee, J. Upcycling of Decommissioned Wind Turbine Blades Through Pyrolysis. *J Clean Prod* 376 134292 (2022) DOI:10.1016/j.jclepro.2022.134292
- [4] Global Offshore Wind Report 2024. Technical Report, from <https://gwec.net/global-offshore-wind-report-2024/>, accessed on 2024-06-01.
- [5] Mishnaevsky Jr, L. Repair of Wind Turbine Blades: Review of Methods and Related Computational Mechanics Problems. *Renew Energ* 140 828-839 (2019) DOI:10.1016/j.renene.2019.03.113
- [6] Savin, A., Iftimie, N., Steigmann, R., Rosu, D., Dobrescu, G.S., Grum, J. et al. Effective Methods for Structural Health Monitoring of Critical Zones of Scalable Wind Turbine Blades. *Stroj Vestn-J Mech E* 64 680-689 (2018) DOI:10.5545/sv-jme.2017.5130
- [7] Fang, H., Feng, Y., Wei, X., Xiong, J. Wind Turbine Blade Damage Aerodynamic Profile Analysis and Its Repair Techniques. *Energ Rep* 9 1-10 (2023) DOI:10.1016/j.egy.2023.04.041
- [8] Cieslak, C., Shah, A., Clark, B., Childs, P. Wind-Turbine Inspection, Maintenance and Repair Robotic System. *ASME Turbo Expo: Power for Land, Sea, and Air* 87127 (2023) DOI:10.1115/GT2023-101713
- [9] Sadeghian, R., Sareh, S. Multifunctional Arm for Telerobotic Wind Turbine Blade Repair. *International Conference on Robotics and Automation* 6883-6889 (2021) DOI:10.1109/ICRA48506.2021.9560968
- [10] Ge J., Deng, Z., Li, W., Li, C. Research Progresses of Robot Grinding and Polishing Force Compliance Controls. *Chin Mech Eng* 32 18 2217-2230 (2021) DOI:10.3969/j.issn.1004-132X.2021.18.011
- [11] Ke, X., Yu, Y., Li, K., Wang, T., Zhong, B., Wang, et al. Review on Robot-Assisted Polishing: Status and Future Trends. *Robot CIM-Int Manuf* 80 (2023) DOI:10.1016/j.rcim.2022.102482
- [12] Guo, W., Yu, S., Tian, Y., Zhao, L., Cao, Z., Active Compliance Constant Force Control with Adaptive Variable Impedance for Robotic Grinding. *J Harbin Inst Tech*, 55 54-65 (2023) DOI:10.11918/202212066
- [13] Lakshminarayanan, S., Kana, S., Mohan, D.M., Manyar, O.M., Then, D., Campolo, D. An Adaptive Framework for Robotic Polishing Based on Impedance Control. *Int J Adv Manuf Technol* 112 401-417 (2021) DOI:10.1007/s00170-020-06270-1
- [14] Zhang, H., Li, L., Zhao, J., Zhao, J. The Hybrid Force/Position Anti-Disturbance Control Strategy for Robot Abrasive Belt Grinding of Aviation Blade Base on Fuzzy PID Control. *Int J Adv Manuf Technol* 114 3645-3656 (2021) DOI:10.1007/s00170-021-07122-2
- [15] Zhang, T., Wu, S., Cai, C. Constant force control method for robotic disk grinding based on floating platform. *J Shanghai Jiaotong Univ* 54 515-523 (2020) DOI:10.16183/j.cnki.jsjtu.2020.05.009
- [16] Wei, Y., Xu, Q. Design of a New Passive End-Effector Based on Constant-Force Mechanism for Robotic Polishing. *Robot Comput-Integr Manuf* 74 102278 (2022) DOI:10.1016/j.rcim.2021.102278
- [17] Zhang, J., Zhao, L., Li, L., Ma, F., Chen, G. Design of passive constant-force end-effector for robotic polishing of optical reflective mirrors. *Chin J Mech Eng* 35 141 (2022) DOI:10.1186/s10033-022-00811-3
- [18] Chen, F., Zhao, H., Li, D., Chen, L., Tan, C., Ding, H. Contact force control and vibration suppression in robotic polishing with a smart end effector. *Robot Comput Integr Manuf* 57 391-403 (2019) DOI:10.1016/j.rcim.2018.12.019
- [19] Xu, D., Lu, X., Xu, B. Design and Modeling of a Passive Magnetic Vibration Absorber for Robotic Polishing Process. *J Manuf Process* 95 204-216 (2023) DOI:10.1016/j.jmapro.2023.03.074
- [20] Li, D., Yang, J., Zhao, H., Ding, H. Contact force plan and control of robotic grinding towards ensuring contour accuracy of curved surfaces. *Int J Mech Sci* 227 107449 (2022) DOI:10.1016/j.ijmecsci.2022.107449
- [21] Mohammad, A.E.K., Hong, J., Wang, D. Design of a force-controlled end-effector with low-inertia effect for robotic polishing using macro-mini robot approach. *Robot Comp-Integr Manuf* 49 54-65 (2018) DOI:10.1016/j.rcim.2017.05.011

- [22] Liang, S., Wei, X., Qi, P., Huang, S., Wang, L. Design of active constant output device based on cylinder. *Opt Precis Eng* 26 640-646 (2018). DOI:10.3788/OPE.20182603.0640 (in Chinese)
- [23] Huang, T., Sun, L., Wang, Z., Yu, X., Chen, G. Hybrid force/position control method for robotic polishing based on passive compliance structure. *Robot* 39 776-785, (2017) DOI:10.13973/j.cnki.robot.2017.0776 (in Chinese)
- [24] Genc, M.O. Cargo e-bike Robust Speed Control Using an MPC Battery Thermal Lumped Model Approach. *Stroj vestn-J Mech E* 70 381-391 (2024) DOI:10.5545/sv-jme.2023.899
- [25] Gao, Z. On the Foundation of Active Disturbance Rejection Control. *Contr Theo Appl* 30 1498-1510 (2013) DOI:10.7641/CTA.2013.31087 (in Chinese)
- [26] Dong, K., Li, J., Lv, M., Li, X., Gu, W., Cheng, G. Active Disturbance Rejection Control Algorithm for the Driven Branch Chain of a Polishing Robot. *Stroj Vestn-J Mech E* 69 509-521 (2023) DOI:10.5545/sv-jme.2023.680
- [27] Liu, F., Wang, L., Jia, X., Mi, J. Application of Linear/Nonlinear Active Disturbance Rejection Switching Control in Variable Load Pneumatic Loading System. *J Mech Eng* 54 225-232 (2018) DOI:10.3901/JME.2018.12.225
- [28] Han, J. From PID to Active Disturbance Rejection Control. *IEEE Trans Ind Electron* 56 900-906 (2009) DOI:10.1109/TIE.2008.2011621

Acknowledgements The research work in this paper was supported by a grant from the Institute of Automation Equipment and Application, Shanghai University of Engineering Science.

Received 2024-08-06, revised 2024-11-12, 2025-01-08, accepted 2025-01-14, Original Scientific Paper.

Data availability The data that underpin the results of this research are available for use by other researchers. Additionally, the corresponding author can provide additional raw data upon reasonable request.

Author contribution Xinrong Liu: supervision, project administration, methodology, writing – review & editing; Hao Li: methodology, formal analysis, validation, writing – original draft; Yu Fang: conceptualization, methodology, writing – review & editing. Diqing Fan: formal analysis, data curation. All authors have contributed significantly to this work and thoroughly reviewed and approved the final version of the manuscript.

Zasnova in vrednotenje pasivne metode nadzora skladnosti robota za brušenje lopatic vetrnih turbin na morju

Povzetek Roboti, ki popravljajo lopatice vetrnih turbin na morju, so dovzetni za motnje različnih dejavnikov, kot je zunanji veter, zaradi česar lahko robot med postopkom brušenja poškoduje lopatice. Zato mora robot v neugodnem delovnem okolju ohranjati konstantno kontaktno silo brušenja. V tej študiji je bila za reševanje tega problema zasnovana naprava za nadzor konstantne sile, ki temelji na pnevmatskem sistemu. Za nadzor te naprave pa je bil predlagan krmilnik, ki temelji na izboljšanem algoritmu ADRC (Active Disturbance Rejection Control). Na podlagi analize mehanizma naprave za nadzor konstantne sile in glede na relativni red sistema je bil zasnovan ADRC algoritem drugega reda. Krmilnik uporablja sledilni diferencial (TD) za filtriranje vhodnega signala, razširjeni opazovalnik stanja (ESO) za oceno celotne motnje v sistemu in nelinearni zakon povratne kontrole napake stanja (NLSEF) za kompenzacijo. Da bi rešili težave z značilnostmi mrtve cone električnega proporcionalnega ventila, neznanimi motnjami med delovanjem na veliki nadmorski višini, spremembami kota nagiba med brušenjem, so bili v krmilnik vključeni algoritmi za kompenzacijo mrtve cone in kompenzacijo težnosti. Na koncu je bila zgrajena eksperimentalna platforma za izvajanje poskusov v različnih delovnih pogojih. Rezultati poskusov kažejo, da krmilnik v primerjavi s tradicionalnim proporcionalno-integralno-derivativnim (PID) algoritmom izboljša čas regulacije sistema za 59 %, pri čemer je prekoračitev blizu nič. V veliki meri sta se zmanjšali tudi absolutna vrednost največje napake in srednja kvadratna vrednost napake. Posledično ima krmilnik boljše natančnost krmiljenja sile in zmogljivost dinamičnega sledenja, močno sposobnost zavračanja motenj in prilagodljivost ter zagotavlja teoretično podlago za praktično inženirsko uporabo.

Ključne besede izboljšani aktivni nadzor zavrnitve motenj, gravitacijska kompenzacija, kompenzacija mrtvega območja, lopatica vetrne turbine na morju, pnevmatski obremenilni sistem